Numerical prediction of flow instabilities in shallow basins

◯ S. Ushijima, ACCMS, Kyoto University, 606-8501, Kyoto, Japan
S. A. Kantoush, DPRI, Kyoto University, 611-0011, Uji-shi, Kyoto, Japan
T. Sumi, DPRI, Kyoto University, 611-0011, Uji-shi, Kyoto, Japan
A. J. Schleiss, LCH, EPFL, 1015 Lausanne, Switzerland

Non-symmetric flow patterns have been observed experimentally under particular geometries even in symmetric shallow rectangular basins. In the present study, it is attempted that the symmetric and non-symmetric flow patterns are numerically simulated with the spatially-filtered Navier-Stokes equations using a standard Smagorinsky model. The governing equations were solved with a finite volume method with a collocated grid system. As a result of the computations, it was shown that the symmetric and non-symmetric flow patterns are successfully predicted in two typical geometries. Meanwhile, there remain some discrepancies between experiments and predictions on velocity distributions, which suggest the necessity to improve the top boundary conditions and subgrid-scale modelings.

1. Introduction

The flow instabilities in wide and shallow open channels have been observed in laboratory experiments [1] and their behaviors were successfully predicted with shallow-water equations [2]. In the present study, the applicability of a three-dimensional computational method is examined when using a standard Smagorinsky model and assuming that the free-surfaces are fixed free-slip boundaries.

The governing equations were solved with a finite volume method with a collocated grid system. A fifth-order non-oscillative conservative scheme was applied to the convection terms of momentum equations in the implicit C-ISMAC [3] method. The pressure fields were calculated with the C-HSMAC method [4], which can keep $|\nabla \mathbf{u}|$ sufficiently small in all fluid cells.

As a result of the computations, it was shown that the symmetric and non-symmetric flow patterns are successfully predicted in two typical geometries. Meanwhile, there remain some discrepancies between experiments and predictions, which suggest the necessity to improve the top boundary conditions and subgrid-scale modelings.

2. Numerical procedures

2.1 Governing equations

The governing equations are spatially-filtered continuity and momentum equations for incompressible Newtonian fluids given by

$$\frac{\partial u_j}{\partial x_j} = 0 \tag{1}$$

$$\frac{\partial u_i}{\partial t} + \frac{\partial}{\partial x_j}(u_i u_j) = f_i - \frac{1}{\rho}\frac{\partial p}{\partial x_i} + \frac{\partial}{\partial x_j}\left(-\tau_{ij} + 2\nu D_{ij}\right) \tag{2}$$

where p and u_i are pressure and filtered velocity component in x_i direction, while ρ, f_i and ν are density, acceleration of body force and kinematic viscosity, respectively, which are all constant values. The strain rate tensor D_{ij} is defined as

$$D_{ij} = \frac{1}{2}\left(\frac{\partial u_i}{\partial x_j} + \frac{\partial u_j}{\partial x_i}\right) \tag{3}$$

A standard Smagorinsky model [5] is utilized to represent τ_{ij} in Eq.(2), which is given by

$$\tau_{ij} = -2\nu_e D_{ij} \tag{4}$$

where ν_e is the turbulent viscosity

$$\nu_e = \left(C_s f_s \Delta\right)^2 |D| \tag{5}$$

with $C_s = 0.173$,

$$\Delta = (\Delta x\ \Delta y\ \Delta z)^{1/3}, \tag{6}$$

and

$$|D| = \sqrt{2 D_{ij} D_{ij}} \tag{7}$$

The damping coefficient f_s is given by

$$f_s = 1 - \exp\left(\frac{-y^+}{A^+}\right) \tag{8}$$

where $A^+ = 25$ and

$$y^+ = \frac{l u_*}{\nu} \tag{9}$$

with the distance l from the nearest wall (except free-slip top boundary), friction velocity u_* and kinematic viscosity ν.

2.2 Discretization and solution method

The numerical procedures of an SMAC method consist of three stages; prediction, pressure-computation and correction stages. At the prediction stage, the tentative velocity components u_i^* are calculated at the center of the fluid-cells with a finite-volume method. In this procedure, Eq.(2) is discretized with the C-ISMAC method [3], which was derived from the implicit SMAC

method [6]. The equation discretized with respect to time is given by

$$\begin{aligned}&\frac{u_i^* - u_i^n}{\Delta t} = f_i - \frac{1}{\rho}\frac{\partial p^n}{\partial x_i} \\ &- \alpha\frac{\partial}{\partial x_j}(u_i^* u_j^n) - (1-\alpha)\frac{\partial}{\partial x_j}(u_i^n u_j^n) \\ &+ \frac{\beta}{\rho}\frac{\partial}{\partial x_j}\left[\frac{\partial}{\partial x_j}(\mu u_i^*) + \frac{\partial}{\partial x_i}(\mu u_j^*)\right] \\ &+ \frac{1-\beta}{\rho}\frac{\partial}{\partial x_j}\left[\frac{\partial}{\partial x_j}(\mu u_i^n) + \frac{\partial}{\partial x_i}(\mu u_j^n)\right] \qquad (10)\end{aligned}$$

where α and β are parameters whose ranges are $0 \leq \alpha, \beta \leq 1$. With the relationship,

$$u_i^* = u_i^n + \tilde{u}_i \qquad (11)$$

Eq.(10) is transformed to the following equation:

$$\begin{aligned}&\frac{\tilde{u}_i}{\Delta t} + \alpha\frac{\partial}{\partial x_j}(\tilde{u}_i u_j^n) - \frac{\beta}{\rho}\frac{\partial}{\partial x_j}\left[\frac{\partial}{\partial x_j}(\mu\tilde{u}_i) + \frac{\partial}{\partial x_i}(\mu\tilde{u}_j)\right] \\ &= f_i - \frac{1}{\rho}\frac{\partial p^n}{\partial x_i} - \frac{\partial}{\partial x_j}(u_i^n u_j^n) \\ &+ \frac{1}{\rho}\frac{\partial}{\partial x_j}\left[\frac{\partial}{\partial x_j}(\mu u_i^n) + \frac{\partial}{\partial x_i}(\mu u_j^n)\right] \qquad (12)\end{aligned}$$

Since $\tilde{u}_i$ is relatively small amplitude compared with u_i^n, we can apply a simple first-order spatial discretization method to the left-hand side of Eq.(12), while a higher-order scheme to the right-hand side. The convection terms are calculated with a fifth-order conservative scheme [7]. The C-ISMAC method enables us to derive easily the simultaneous equation system from the implicit form of the left-hand side of Eq.(12) as well as to preserve numerical accuracy by applying a higher-order scheme to the explicit form on the right-hand side of the same equation.

After solving the equation system of $\tilde{u}_i$, which is derived from the discretized equation of Eq.(12), u_i^* is determined with Eq.(11). The u_i^* located at the center of the fluid-cell is then spatially interpolated on the cell boundary. Before this interpolation, pressure-gradient term calculated at the cell center is removed from u_i^* in order to prevent pressure oscillation as

$$\hat{u}_i = u_i^* + \frac{1}{\rho}\frac{\partial p^n}{\partial x_i}\Delta t \qquad (13)$$

The cell-center velocity $\hat{u}_i$, which is calculated without the pressure-gradient term, is spatially interpolated on the cell boundaries by a suitable function f_b. After this procedure, the pressure-gradient terms that are estimated on the cell boundaries are added to the interpolated velocity, $f_b(\hat{u}_i)$. Thus, we obtain the cell-boundary velocity component $u_{b,i}$ as follows:

$$u_{b,i} = f_b(\hat{u}_i) - \frac{1}{\rho}\left.\frac{\partial p^n}{\partial x_i}\right|_b \Delta t \qquad (14)$$

The velocity component $u_{b,i}^{n+1}$ at $n+1$ time-step is defined by

$$u_{b,i}^{n+1} = f_b(\hat{u}_i) - \frac{1}{\rho}\left.\frac{\partial p^{n+1}}{\partial x_i}\right|_b \Delta t \qquad (15)$$

Subtracting Eq.(14) from Eq.(15), we have

$$u_{b,i}^{n+1} = u_{b,i} - \frac{1}{\rho}\frac{\partial \phi}{\partial x_i}\Delta t \qquad (16)$$

where $\phi = p^{n+1} - p^n$. Substitution of Eq.(16) into Eq.(1) yields the following equation of ϕ :

$$\frac{\partial}{\partial x_i}\left(\frac{1}{\rho}\frac{\partial \phi^k}{\partial x_i}\right) = \frac{1}{\Delta t}\frac{\partial u_{b,i}}{\partial x_i} \equiv \frac{\nabla \boldsymbol{u}}{\Delta t} \qquad (17)$$

At the pressure-computation stage, Eq.(17) is solved with the C-HSMAC method [4]. The C-HSMAC method enables us to obtain the pressure and cell-boundary velocity components, which satisfy the incompressible condition $|\nabla \boldsymbol{u}| < \epsilon_D$ in each computational cell, where ϵ_D is a given threshold. While the final results of the C-HSMAC method are similar to those of the SOLA method [8], it has been proved that the computational efficiency of the C-HSMAC method is largely improved. The relationships in the C-HSMAC method are given by

$$\frac{\partial}{\partial x_i}\left(\frac{1}{\rho}\frac{\partial \phi}{\partial x_i}\right) = \frac{\nabla \boldsymbol{u}^k}{\Delta t} \qquad (18)$$

$$p^{k+1} = p^k + \phi \qquad (19)$$

$$u_{b,i}^{k+1} = u_{b,i}^k - \frac{\Delta t}{\rho}\frac{\partial \phi}{\partial x_i} \qquad (20)$$

where the superscript k stands for the iteration step-number of the C-HSMAC method.

The discretization of Eq.(18) yields simultaneous linear equation system of ϕ, which is solved with the BiCGSTAB method [9]. The iterative computation using the above three equations is completed when $|\nabla \boldsymbol{u}| < \epsilon_D$ is satisfied in all fluid-cells.

3. Applicability of prediction method

3.1 Computational conditions

Fig.1 shows the plane view of the rectangular basin, to which the present computational method was applied. The origin of the orthogonal coordinates is set on the bottom of the upstream right hand side corner, where x, y and z are streamwise, transverse and vertically-upward directions, respectively. Computations were performed for two geometries, case-3×4 and case-6×2, in which a pair of the lengths (L, B) shown in Fig.1 are (3m, 4m) and (6m, 2m), respectively. The depth of water is 0.2 m in both cases. The average inlet velocity u_0 is 0.14 m/s. In the computations, as shown in Fig.2, the additional zones were set up on upstream and downstream boundaries to simulate the channels used in experiments, whose longitudinal lengths are both 0.5 m.

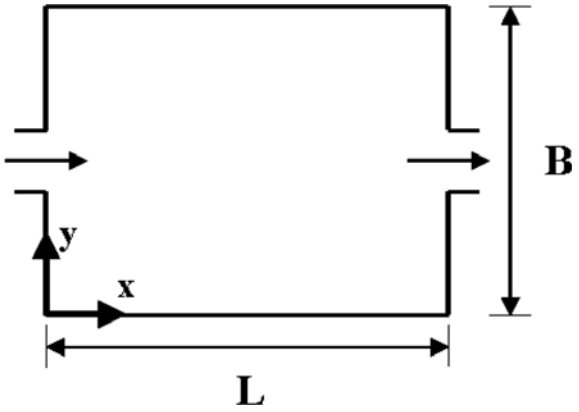

Fig. 1: Plane view of rectangular basin and coordinates

Fig. 2: 3D computational area

The numbers of fluid cells in computations in (x, y, z) directions are $160\times160\times8$ for case-3×4 and $280\times80\times8$ for case-6×2 including the four boxes on the corners shown in Fig.2. All boundaries are treated as non-slip walls except top boundary that is a fixed free-slip wall. The inlet velocity is $u_{in} = u_0 + u'$, where u' is the fluctuation component given with the uniform random number ranging from $-0.2u_0$ to $0.2u_0$. The pressure boundary conditions are given by $\partial p/\partial x = 0$ except the outlet boundary. On the other hand, $\partial u/\partial x = 0$ and $p = 0$ are imposed on the outlet boundary of the downstream channel.

The computations start from initial static flow field at $t = 0$ until $t = 1{,}000$ sec. with the time increment $\Delta t = 2.5 \times 10^{-2}$ sec. Since the grid-scale flow fields are obtained at each time step, the averaged results are calculated from $t = 800$ to 1,000 sec.

Fig.3 shows the view of the calculated results in case-6×2, which are averaged values during the above time period. As shown in this figure, while 3D results are obtained in the predictions, 2D velocity fields on top boundaries are mainly used in the comparisons with experiments.

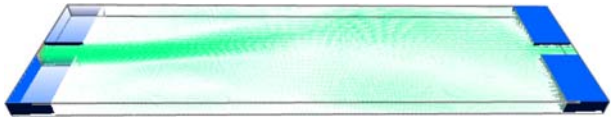

Fig. 3: Averaged 3D flow patterns of predicted results (case-6×2)

3.2 Comparison with experimental results

Figs.4 and 5 show the two-dimensional flow patterns in case-3×4 on the top surfaces obtained in experiments [(1)] and predictions, respectively. In this case, it can be seen that the symmetric flow patterns arise in experiments and calculations.

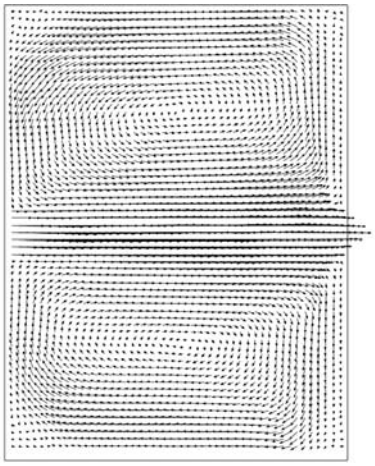

Fig. 4: Experimentally-observed flow patterns on free-surface (case-3×4)

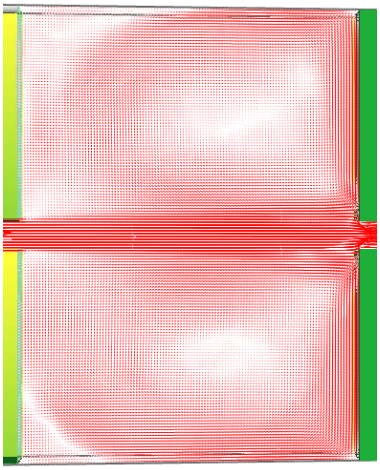

Fig. 5: Averaged 2D flow patterns of predicted results on top boundary (case-3×4)

On the other hand, Figs.6 and 7 show the similar 2D flow patterns for case-6×2. In this case, non-symmetric patterns appear in both experiments and predictions. Whilst the main flows attach on the left-hand side in the computations, which is upside-down compared with experiments, it is not an essential problem, since the attached side is not deterministic depending on the instabilities in the flows.

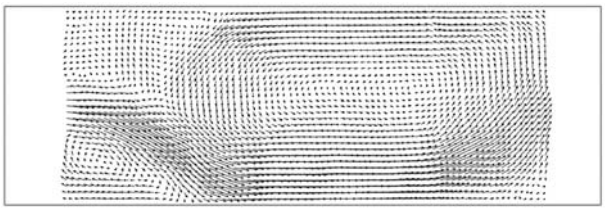

Fig. 6: Experimentally-observed flow patterns on free-surface (case-6×2)

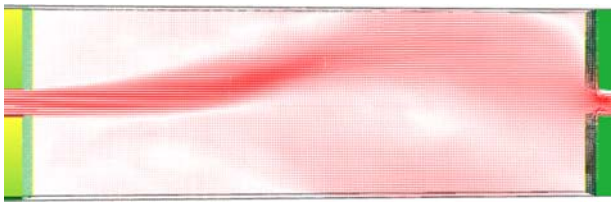

Fig. 7: Averaged 2D flow patterns of predicted results on top boundary (case-6×2)

Fig.8 show the predicted unsteady flow patterns for case-3×4 on the top boundary. As shown in these figures, the incoming flows impinge on the downstream side and then two circulating flows are formed on both sides of the main stream. While some organized eddy motions are found in the snapshots of Fig.8, the overall flow patterns are preserved until 1,000 sec. This results in the averaged velocity field shown in Fig.5, which is nearly symmetric similarly to the experiments shown in Fig.4.

The development of non-symmetric flow patterns for case-6×2 is shown in Fig.9. As shown in Figs.9 (a) to (d), the initial average flow field is approximately symmetric, while a large circulating flow arises after around $t = 250$ s. and then the main flow patterns become non-symmetric.

Figs.10 to 12 show the distribution of u along y direction for case-3×4 on the sections of $x = 1.0$, 1.5 and 2.0 m, respectively. The predicted results seem to be less diffusive and have more large velocity gradients compared with experiments.

Figs.13 to 15 shows the similar velocity distributions for case-6×2 on the sections of $x = 1.5$, 3.0 and 4.5 m, respectively. In this case, it can be seen that the predicted inlet flow tends to progress more straightly and its distance to the reattachment point is larger compared with experiments. As a result of the quantitative comparisons, some discrepancies are found in the velocity distributions. This fact might suggest that the necessity to improve the treatment of free-surface boundary conditions and subgrid-scale modelings.

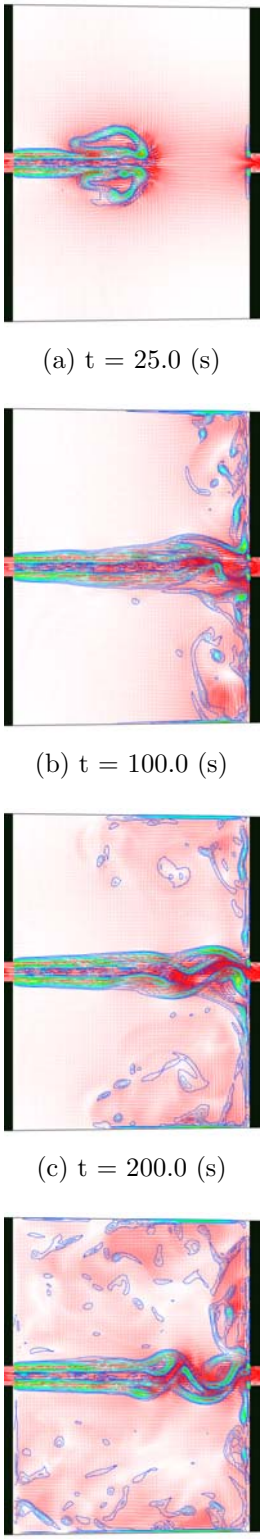

(a) t = 25.0 (s)

(b) t = 100.0 (s)

(c) t = 200.0 (s)

(d) t = 1000.0 (s)

Fig. 8: Predicted flow patterns and isolines for 2D vorticities on top surface (case-3×4)

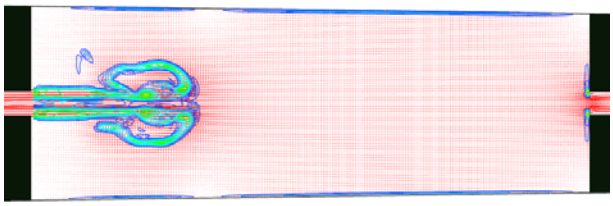

(a) t = 25.0 (s)

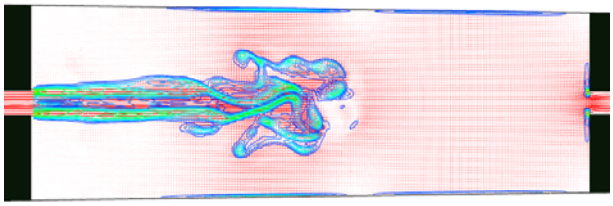

(b) t = 50.0 (s)

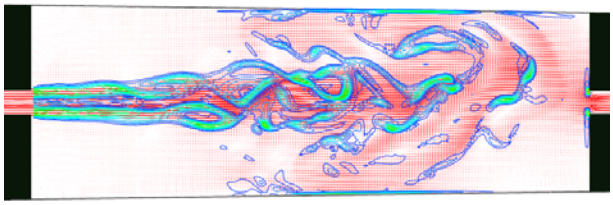

(c) t = 100.0 (s)

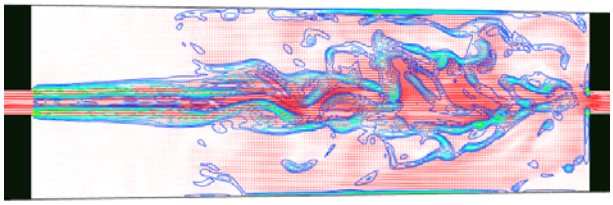

(d) t = 150.0 (s)

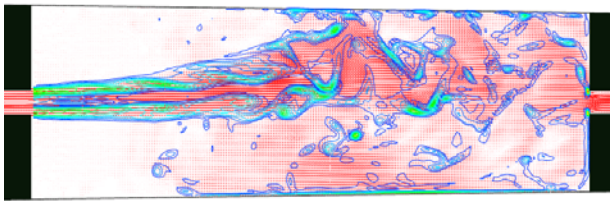

(e) t = 250.0 (s)

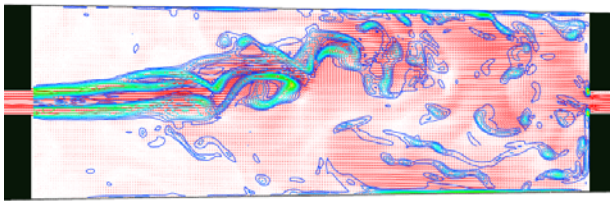

(f) t = 1000.0 (s)

Fig. 9: Predicted flow patterns and isolines for 2D vorticities on top surface (case-6×2)

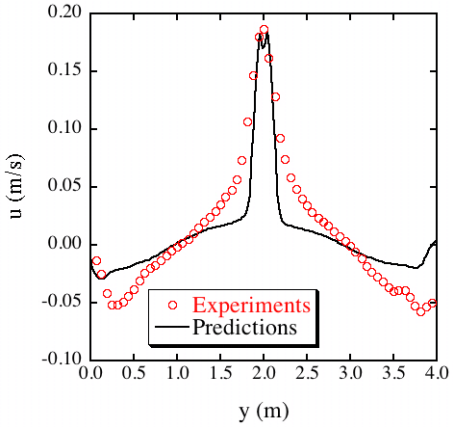

Fig. 10: Distribution of u in section $x = 1.0$ (m) (case-3×4)

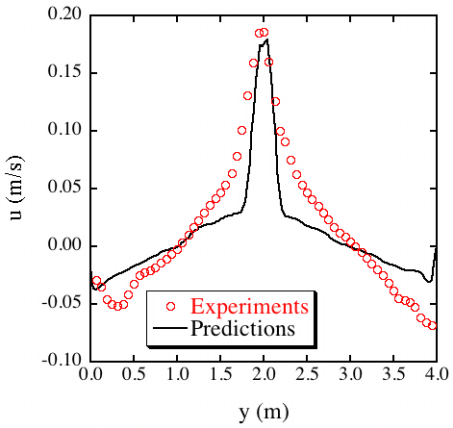

Fig. 11: Distribution of u in section $x = 1.5$ (m) (case-3×4)

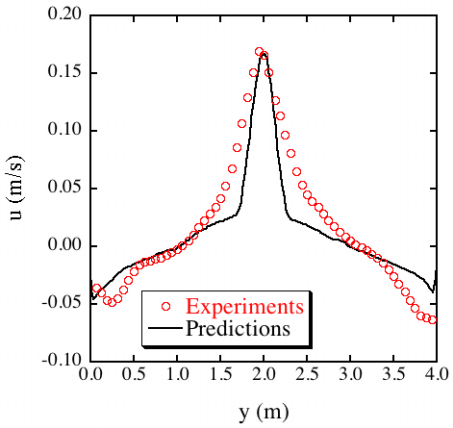

Fig. 12: Distribution of u in section $x = 2.0$ (m) (case-3×4)

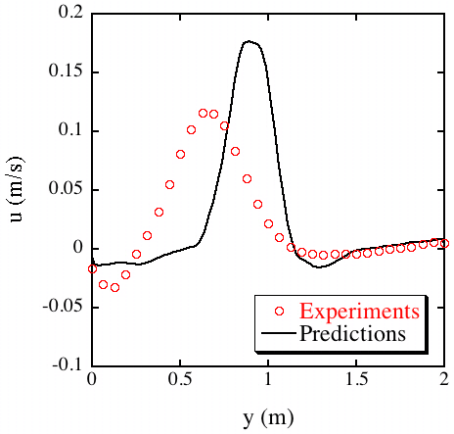

Fig. 13: Distribution of u in section $x = 1.5$ (m) (case-6×2)

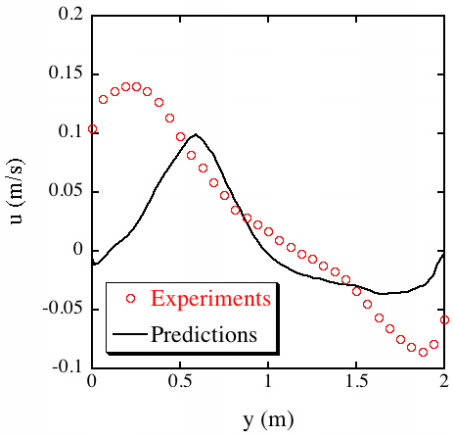

Fig. 14: Distribution of u in section $x = 3.0$ (m) (case-6×2)

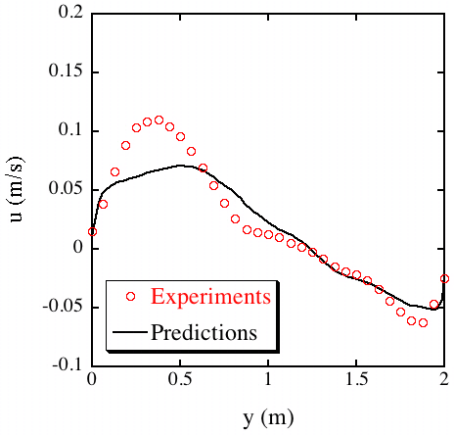

Fig. 15: Distribution of u in section $x = 4.5$ (m) (case-6×2)

Conclusions

Two typical flow patterns observed in rectangular basins were numerically simulated with the spatially-filtered Navier-Stokes equations using a standard Smagorinsky model. The governing equations were solved with a finite volume method with a collocated grid system. As a result, it was shown that the symmetric and non-symmetric flow patterns are successfully predicted in two cases. On the other hand, some discrepancies were found in the velocity distributions between experiments and calculations. In the future studies, it is suggested that more investigations may be necessary to improve the treatment of free-surfaces and subgrid-scale models.

Acknowledgments

The authors are grateful to Mr. H. Yamashita for his enormous contribution to this study.

References

1. S. A. Kantoush. Symmetric or asymmetric flow patterns in shallow rectangular basins with sediment transport. *Proc. 32nd IAHR biennial congress*, 2007.

2. B. J. Dewals, S. A. Kantoush, S. Erpicum, M. Pirotton, and A. J. Schleiss. Experimental and numerical analysis of flow instabilities in rectangular shallow basins. *Environ Fluid Mech.*, Vol. 8, pp. 31–54, 2008.

3. S. Ushijima and I. Nezu. Higher-order implicit (C-ISMAC) method for incompressible flows with collocated grid system. *JSCE Journal*, No. 719/II-61, pp. 21–30, 2002.

4. S. Ushijima and Y. Okuyama. Comparison of C-HSMAC and SOLA methods for pressure computation of incompressible fluids. *JSCE Journal*, No. 747/II-65, pp. 197–202, 2003.

5. J. Smagorinsky. General circulation experiments with the primitive equations. *Monthly Weather Review*, Vol. 91, No. 3, pp. 343–368, 1963.

6. B. R. Shin, T. Ikohagi, and H. Daiguji. An unsteady implicit SMAC scheme for two-dimensional incompressible Navier-Stokes equations. *JSME International Journal*, Vol. 36, No. 4, pp. 598–606, 1993.

7. S. Yamamoto and H. Daiguji. Higher-order-accurate upwind schemes for solving the compressible Euler and Navier-Stokes equations. *Computers Fluids*, Vol. 22, No. 2/3, pp. 259–270, 1993.

8. C. W. Hirt and J. L. Cook. Calculating three-dimensional flows around structures and over rough terrain. *J. Comput. Phys.*, Vol. 10, pp. 324–340, 1972.

9. H. A. Van Der Vorst. BI-CGSTAB : A first and smoothly converging variant of BI-CG for the solution of nonsymmetric linear systems. *SIAM J. Sci. Stat. Comput.*, Vol. 13, pp. 631–644, 1992.